PERGAMON

International Journal of Heat and Mass Transfer 45 (2002) 2021–2030

International Journal of HEAT and MASS TRANSFER

www.elsevier.com/locate/ijhmt

Accuracy of measurements of curvature and apparent contact angle in a constrained vapor bubble heat exchanger

Ling Zheng, Ying-Xin Wang, Joel L. Plawsky, Peter C. Wayner, Jr. *

The Isermann Department of Chemical Engineering, Rensselaer Polytechnic Institute, 110 8th Street, Troy, NY 12180-3590, USA

Received 3 January 2001; received in revised form 28 September 2001

Abstract

Improved experimental and analytical techniques were developed to measure the liquid pressure field in a meniscus formed in the right angled corner of a Constrained Vapor Bubble (CVB) heat exchanger. Based on the definition of the curvature, an analytical expression for the curvature as a function of the film thickness profile and the apparent contact angle was obtained. The error associated with the resolution of the image processing system was defined and several imaging factors affecting the error are discussed. The error associated with the system resolution, E_r, increases as the curvature increases; the apparent contact angle increases; the wavelength decreases; and the number of dark fringes used for the data fitting decreases. The accuracy of the data fitting can be used to also determine the region where the disjoining pressure and viscous stresses affect the results. Examples using pentane data are presented. The relatively large experimental cell size with regions of low capillary pressure was dictated by future use in microgravity.

Keywords: Evaporation; Meniscus; Capillarity; Interferometry; Contact angle

1. Introduction

The gradient in the liquid pressure, and the pressure and temperature differences at the liquid–vapor interface control fluid flow and phase change heat transfer processes in pure microscale liquid–vapor systems like an evaporating extended meniscus (e.g., theoretically discussed in [1–15] and experimentally discussed in [16–28]). Since the accuracy of the measured interfacial vapor pressure field is a function of errors in the measurement of the shape, temperature, gravitational force and composition of the system, this accuracy must be evaluated to understand the above and future results. The use of models comparing the Clapeyron effect and Kelvin effect on vapor pressure demonstrate that it should be easier to measure the effect of the interfacial pressure jump on the transport processes than the effect of local temperature changes [27,28]. Experimental results are directly related to the errors associated with the resolution of the image processing system used to obtain the pressure jump. Herein, we discuss improved analytical techniques to determine the curvature field from thickness profile data in both equilibrium and evaporating menisci formed in the right angled corner of a Constrained Vapor Bubble (CVB) heat exchanger. Based on the definition of the curvature, an analytical expression for the apparent contact angle and the curvature as a function of the optically measured film thickness profile is presented. The results evaluate the usefulness of the image processing technique to measure pressure fields and, thereby, transport processes.

Capillary fluid flow in a right angled corner is important to many engineering devices. Related research includes extensive studies on the behavior of liquid films in the grooves of heat transfer devices [3,9,29–31]. Using interfacial concepts like the Kelvin, Young–Dupre, and augmented Young–Laplace equations, models have been developed for interfacial fluxes in the contact line region [26]. Ayyaswamy et al. [3] obtained solutions to the two-dimensional equations of motion governing steady laminar flow in a triangular groove with the free

* Corresponding author. Tel.: +1-518-276-6199; fax: +1-518-276-4030.

E-mail address: wayner@rpi.edu (P.C. Wayner Jr.).

0017-9310/02/$ - see front matter
PII: S0017-9310(01)00306-4

Nomenclature

a	inside dimension of the cell
Ac	accuracy of the data fitting
C	constant
C_l	geometric coefficient
c	liquid film length in corner
E_r	error due to the resolution of the system
g	acceleration of gravity
ΔH	latent heat of vaporization
k_f	friction factor coefficient
K	curvature
l	axial distance
M	molecular weight
N	total number of dark and bright fringes
n_l	refractive index of the liquid
P	pressure
R	gas constant
r	radius of curvature
Y	distance between consecutive dark fringes
y	radial direction

Greek symbols

Γ	mass flow rate
δ	film thickness
θ_c	apparent contact angle
Π	disjoining pressure
ρ	density
σ	surface tension

Subscripts

1,2	arbitrary number of location index
$\perp$	perpendicular to the axis of the cell
$\parallel$	parallel to the axis of the cell
b	base of the CVB
exp	experimental data
h	defined in Eqs. (3) and (4)
i	average value
l	liquid
m	mth order of dark fringe
n	nth order of dark fringe
lv	liquid–vapor interface
theo	theoretical results
v	vapor
vx	vapor at x

Superscripts

C	Clapeyron effect
g	hydrostatic effect
K	Kelvin effect

surface governed by surface tension forces. Xu and Carey [9] used an analytical model to predict the heat transfer characteristics of film evaporation on a microgroove surface. Stephan and Busse [10] presented a model for the radial heat transfer in a grooved heat pipe evaporator. Swanson and Herdt [11] developed a mathematical model of the evaporating extended meniscus in a V-shaped channel to investigate the effect of wedge half-angle and vapor mass transfer on meniscus morphology, fluid flow, and heat transfer. Khrustalev and Faghri [29] developed a mathematical model to describe heat transfer through thin liquid films in the evaporator of heat pipes with capillary grooves. These studies provide valuable information on the mechanism of the evaporating flow in microgrooves. However, few experimental investigations as those discussed herein have been done to measure simultaneously both the curvature and apparent contact angle of a liquid meniscus, which then give the pressure and flow fields in a heat exchanger. We find that experimental accuracy is particularly important in the measurement and interpretation of the film profile. Discussion and evaluation of this accuracy is one of the main objectives of this paper.

Fig. 1 shows a schematic drawing of the vertical experimental CVB setup which was used. The details of the design were essentially given in Wang et al. [27] and are only briefly described here. The current CVB is formed

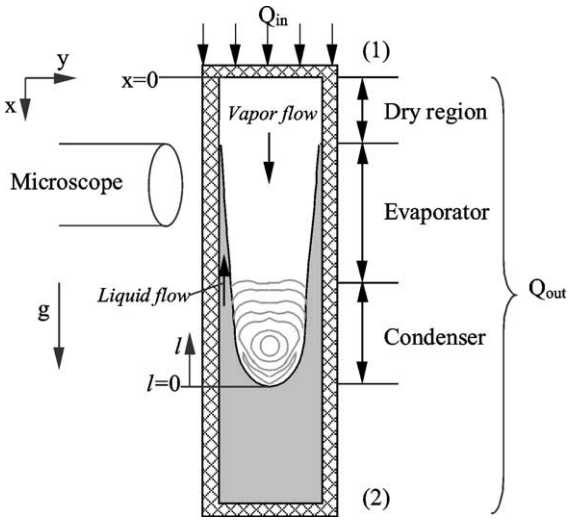

Fig. 1. A schematic drawing of the vertical CVB.

by underfilling a square cross-sectional cell with inside dimensions of 3 mm × 3 mm × 40 mm initially under vacuum with 99.9% pure pentane. The relatively large size, which gives regions of low capillary pressure and low viscous losses was dictated by planned use in future microgravity experiments. The transparent wall of the quartz CVB heat exchanger allows the pressure field of

the fluid in the corner to be measured optically through a microscope using naturally occurring interference fringes [31]. If temperature $T_1 > T_2$, energy flows from End (1) towards End (2) by conduction in the walls and by an evaporation, vapor flow and condensation mechanism. The right angled corners of the CVB cell act as liquid arteries where the condensate flows towards End (1) because of the axial pressure gradient which is a function of the film profile. Perpendicular to the axis, there is a transverse component of the pressure gradient causing flow towards the contact line of the meniscus. The axial temperature profile was obtained using small thermocouples attached to the flat surface of the cell at 2 mm intervals. The thermocouples are not shown in the figure. Energy is lost to the surroundings by a natural convection process along the entire length of the cell. In essence, the cell is a large scale version of a micro heat pipes [14,32]. Since the cell is designed for use in microgravity, the large dimensions are an advantage because of the reduced liquid viscous losses. The vapor space is almost isobaric.

The cross-section of the CVB cell is given in Fig. 2. There is a shape dependent "pressure jump" at the vapor–liquid interface, $P_v - P_l$, due to the anisotropic stress tensor near interfaces. The pressure jump is given by the following extended Young–Laplace equation which includes the effects of both capillarity (σK) and thickness dependent disjoining pressure (Π).

$$P_v - P_l = \sigma K + \Pi, \tag{1}$$

where K is the curvature, and Π is the disjoining pressure [1,2]. The curvature of the liquid meniscus in the corner changes continually along the axial length of the cell due to the viscous losses, gravity and the evaporation/condensation processes. The main objectives of this paper are to present an improved image analyzing technique based on interferometry for obtaining both the curvature and apparent contact angle, an error analysis of the technique and examples of experimental results. Although the evaluation of the microscopic details of both the pressure and temperature fields are important, this paper emphasizes the measurements of the pressure field which is amenable to experimental measurement. The microscopic details of the interfacial temperature field need to be numerically determined which is beyond the scope of this paper.

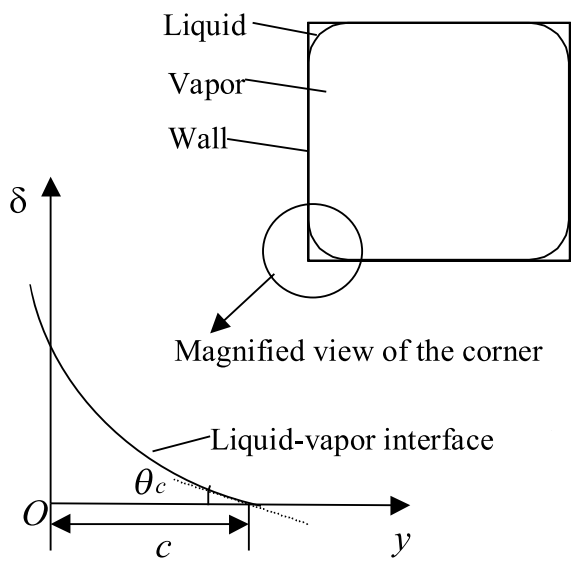

Fig. 2. Cross-section of the CVB cell at x.

The presented technique is an improvement of the following previous uses of interferometry in change of phase heat transfer. Sharp [16] used the interference of monochromatic light reflected at the liquid–vapor and liquid–solid interfaces in a thin liquid film to visualize an evaporation liquid film at the base of bubbles on glass during nucleate boiling. Jawurek [17] analyzed the interference fringe patterns of microlayers to determine the detailed shape and thickness of the microlayer. Voutsinos and Judd [18] investigated the growth and evaporation of the microlayer underlying a bubble forming on a glass heater surface using laser interferometry and high speed photography. Using interferometry, Renk and Wayner [19] measured the profile of an evaporating ethanol meniscus as a function of the evaporative heat flux. Yang and Nouri [33] used laser shawdowgraphy to study surface tension effects in evaporating drops on a flat surface. Wayner et al. [21] studied evaporation in the contact line region of a thin film of hexane on a silicon wafer using interferometry. Chen and Wada [34] studied the isothermal spreading dynamics of a drop edge using a laser light interference microscopy method. Kihm and Pratt [26] presented a Fizeau interferometry technique to determine the contours of thin film thickness variations of evaporating pentane menisci. DasGupta et al. [31] and Karthikeyan et al. [25] used image analyzing interferometry to measure curvatures of a completely wetting liquid film. Under the assumption that the square of the slope, $(\mathrm{d}\delta/\mathrm{d}y)^2$, was very small compared to one, the curvature was obtained in [25,31] from the slope of the plot of the square root of the film thickness ($\mathrm{d}\delta^{1/2}/\mathrm{d}y$). For the isothermal CVB with a small inclination angle and the intermediate region of the non-isothermal CVB, the curvatures were relatively small and the experimental data agreed well with the theoretical results. However, with high evaporation rates and/or with partially wetting liquids, an improved analyzing technique is needed since the value of $(\mathrm{d}\delta/\mathrm{d}y)^2$ becomes too large. Therefore, using the definition of the curvature, an improved analytical expression for the curvature as a function of the film thickness profile and the apparent contact angle was obtained and is presented herein. This

expression can be used to obtain simultaneously the curvature and the apparent contact angle for a curved film of either a partially wetting fluid or completely wetting fluid in the region where disjoining pressure can be neglected. The subsequent accuracy analysis of the data fitting algorithm can be used to also determine the region where the disjoining pressure affects the results.

2. Effect of temperature and pressure on the local interfacial heat flux

Using Eqs. (16) and (17) in the analysis by Wayner [35], the local vapor pressure jump at the liquid–vapor interface and the local change of phase interfacial heat flux are

$$P_{\mathrm{lv}} - P_{vx} = -\frac{V_{\mathrm{l}}P_{\mathrm{v}}}{RT_{\mathrm{lv}}}[\Pi + \sigma_{\mathrm{lv}}(K - K_{\mathrm{b}})] + \frac{V_{\mathrm{l}}M\Delta HP_{\mathrm{v}}}{RT_{\mathrm{lv}}T_{\mathrm{v}}} \times (T_{\mathrm{lv}} - T_{\mathrm{v}}) + \frac{MgP_{\mathrm{v}}}{RT_{\mathrm{v}}}l, \tag{2}$$

$$q'' = C\left(\frac{M}{2\pi RT_i}\right)^{1/2}\left\{\frac{P_{\mathrm{v}}M\Delta H^2}{RT_{\mathrm{v}}T_{\mathrm{lv}}}(T_{\mathrm{lv}} - T_{\mathrm{v}}) - \frac{V_{\mathrm{l}}P_{\mathrm{v}}\Delta H}{RT_{\mathrm{lv}}}[\Pi + \sigma_{\mathrm{lv}}(K - K_{\mathrm{b}})] + \frac{MgP_{\mathrm{v}}\Delta H}{RT_{\mathrm{v}}}l\right\}, \tag{3}$$

$$q'' = h_{\mathrm{lv}}^{\mathrm{C}}(T_{\mathrm{lv}} - T_{\mathrm{v}}) - h_{\mathrm{lv}}^{\mathrm{K}}[\Pi + \sigma_{\mathrm{lv}}(K - K_{\mathrm{b}})] + h_{\mathrm{lv}}^{\mathrm{g}}l. \tag{4}$$

Using pentane at $T = 25$ °C, the values of the coefficients are $h_{\mathrm{lv}}^{\mathrm{C}} = 4.66 \times 10^7$, $h_{\mathrm{lv}}^{\mathrm{K}} = 5.12$, $h_{\mathrm{lv}}^{\mathrm{g}} = 3.72 \times 10^5$. These values along with the relative ease of obtaining microscopic thickness profiles demonstrate that the microscopic effect of the pressure field is easier to evaluate experimentally than the temperature field.

2.1. Effect of gravity and curvature on axial transport

Using Eq. (4) with $T_{\mathrm{lv}} = T_{\mathrm{v}}$ and $q'' = 0$ gives

$$\Pi + \sigma_{\mathrm{l}}(K - K_{\mathrm{b}}) = -\rho_{\mathrm{l}}gl, \tag{5}$$

where l is the distance between an axial location and the bottom of the vapor bubble. Note that $g < 0$ in this section. In the thicker portion of the meniscus ($\delta > 0.1$ μm) the disjoining pressure can be neglected and the local curvature in the corner is

$$K = K_{\mathrm{b}} - \frac{\rho_{\mathrm{l}}gl}{\sigma_{\mathrm{l}}}. \tag{6}$$

This simple hydrostatic result is confirmed experimentally below.

Since the disjoining pressure for pentane is proportional to $1/\delta^n$ (n is 3 or 4) [35], $\Pi = 0$ at the base of the CVB, where the film is very thick, the curvature is two-dimensional and the radius of curvature parallel to the CVB axis ($r_{\parallel}$) is equal to that normal to the CVB axis ($r_{\perp}$). Hence, in our case,

$$K_{\mathrm{b}} = \frac{1}{a/2} + \frac{1}{a/2} = \frac{4}{a} = 1333\ \mathrm{m}^{-1},$$

where $a = 3$ mm is the inside dimension of the cell. At a location far away from the base, $r_{\parallel} >> r_{\perp}$, thus, the mean curvature is $K = 1/r_{\perp}$.

For a non-isothermal CVB, the axial gradient in the curvature where $\delta > 0.1$ μ m can be related to the axial mass flow rate in that portion of the meniscus [36].

$$\Gamma = -\frac{C_{\mathrm{l}}^3}{K^4\nu k_{\mathrm{f}}}\frac{\mathrm{d}}{\mathrm{d}l}(\sigma_{\mathrm{l}}K + \rho_{\mathrm{l}}gl). \tag{7}$$

Since the gravitational effect is unimportant in microgravity, the axial transport processes are larger under these conditions and large fluxes are predicable for large systems with small axial viscous losses. Viscous effects perpendicular to the gravity vector in the thinner portion of the meniscus remain the same.

2.2. Use of film profile to obtain curvature and apparent contact angle

As shown in Fig. 2, the liquid–vapor interface is symmetric on reflection in the four corners of the CVB cell. With a completely wetting liquid or partially wetting liquid forming a concave liquid film in the corner, a cartesian coordinate system is established for one of the corners. An apparent finite contact angle of θ_{c} forms on the interior wall of the container, and c is the liquid–wall contact line length. The apparent equilibrium contact angle is defined as the angle where the extrapolated constant curvature liquid–vapor interface meets the solid.

In the region, where $\Pi = 0$, the constant curvature (K) of the equilibrium liquid film in the corner at a particular axial location is defined as

$$K = \frac{\frac{\mathrm{d}^2\delta}{\mathrm{d}y^2}}{\left[1 + \left(\frac{\mathrm{d}\delta}{\mathrm{d}y}\right)^2\right]^{3/2}}, \tag{8}$$

where δ represents the film thickness of the liquid, y represents the corresponding location in the film profile. Assuming that the curvature of the curved liquid film is constant, integrating equation (8) gives

$$\frac{\delta'}{\sqrt{1 + (\delta')^2}} = Ky + C_1, \tag{9}$$

where C_1 is a constant and $\delta' = \mathrm{d}\delta/\mathrm{d}y$. The boundary conditions for Eq. (8) are

$$y = c, \quad \delta = 0, \quad \delta' = \tan(\pi - \theta_{\mathrm{c}}). \tag{10}$$

Substituting the boundary conditions into Eq. (9), $C_1 = -\sin\theta_c - Kc$. Integrating equation (9) leads to

$$\delta = -\frac{\sqrt{1-(Ky+C_1)^2}}{K} + C_2, \tag{11}$$

where $C_2 = \cos\theta_c/K$. Hence, the film thickness is expressed as the following function of the curvature and apparent contact angle

$$\delta = \frac{-\sqrt{1-(Ky-Kc-\sin\theta_c)^2}+\cos\theta_c}{K}. \tag{12}$$

Rearranging Eq. (12), the location of the film thickness can be written as

$$y = c + \frac{\sin\theta_c}{K} - \sqrt{\frac{1}{K^2} - \left(\frac{\cos\theta_c}{K} - \delta\right)^2}. \tag{13}$$

The experimental film profile, δ vs. y, is obtained from naturally occurring interference fringes which result from the reflection of monochromatic light at both the liquid–vapor and liquid–solid interfaces (e.g., [31]). The two unknowns, K and θ_c, can be obtained simultaneously by best fitting the experimental film thickness profile, $\min(\sum_{i=1}^{N}(y_{\exp,i} - y_{\mathrm{theo},i})^2)$, where N is the total number of dark and bright fringes. The subscripts exp and theo denote the experimental data and theoretical values obtained from Eq. (13), respectively. Note that the liquid–wall contact line length, c, in Eq. (13) is canceled out during the data fitting since only the relative distances between the fringes to the first fringe are needed. Eq. (13) is used below to obtain the curvature of a concave film in the corner of the cell. Wang et al. [28] extended it to obtain the curvatures of sessile drops in studies of droplet condensation, and demonstrated that the condensate removal rate was a function of the curvature and contact angle, which self-adjust to give the necessary force field.

3. Error analysis

Using Eq. (13), the distance between the mth dark fringe and the nth dark fringes is

$$Y \equiv |y_m - y_n| = \left| \sqrt{\frac{1}{K^2} - \left(\delta_m - \frac{\cos\theta_c}{K}\right)^2} - \sqrt{\frac{1}{K^2} - \left(\delta_n - \frac{\cos\theta_c}{K}\right)^2} \right|, \tag{14}$$

where δ_m and δ_n are the film thickness of the mth and nth dark fringes,

$$\delta_m = \frac{(2m+1)\lambda}{4n_l} \quad \text{and} \quad \delta_n = \frac{(2n+1)\lambda}{4n_l}.$$

Differentiating equation (14) with respect to K yields

$$\frac{\mathrm{d}Y}{\mathrm{d}K} = \left| \frac{\left[-\frac{1}{K^3} - \left(\delta_m - \frac{\cos\theta_c}{K}\right)\frac{\cos\theta_c}{K^2}\right]}{\sqrt{\frac{1}{K^2} - \left(\delta_m - \frac{\cos\theta_c}{K}\right)^2}} - \frac{\left[-\frac{1}{K^3} - \left(\delta_n - \frac{\cos\theta_c}{K}\right)\frac{\cos\theta_c}{K^2}\right]}{\sqrt{\frac{1}{K^2} - \left(\delta_n - \frac{\cos\theta_c}{K}\right)^2}} \right|. \tag{15}$$

The error due to the resolution of the system, E_r, is computed as

$$E_r = \frac{\frac{\mathrm{d}K}{\mathrm{d}Y} Y_r}{K}, \tag{16}$$

where Y_r is the resolution of the image processing system. The resolution of our current system is $Y_r = 0.1777$ μm/pixel which was obtained experimentally using a standard chrome-on-glass calibrated resolution target. It is evident from Eqs. (15) and (16) that the value of E_r depends on the system resolution, the number of dark fringes used to obtain the curvature, the apparent contact angle (θ_c), the wavelength (λ), and the refractive index of the liquid (n_l). To demonstrate the effects of these factors, Figs. 3 and 4 are shown below with curvatures ranging from 1000 to 2.5×10^4 m^{-1}. We choose this moderate range because the curvature in the condenser can be as small as 1000 m^{-1} and the measurable curvature in the evaporator can be very large. For example, with our current equipment, it can be measured up to approximately 5.5×10^4 m^{-1}. Finally, there can be additional errors due to variations in

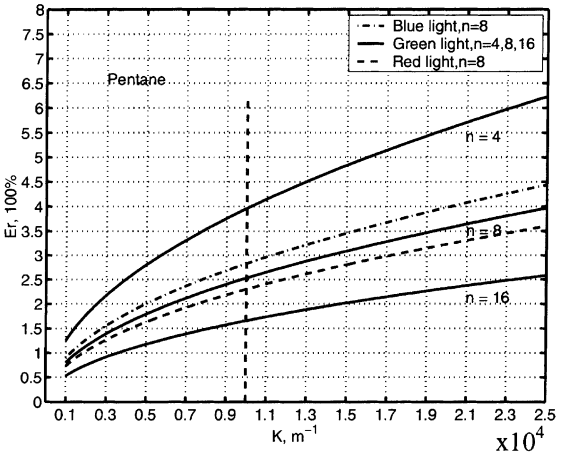

Fig. 3. Effects of wavelength and the number of dark fringes on the error of the curvature measurements for $\theta_c = 0$.

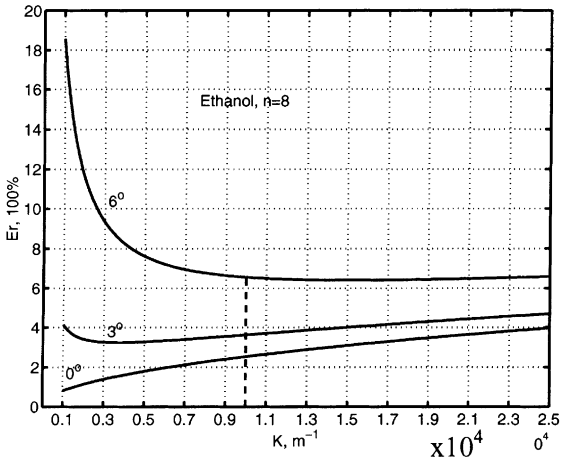

Fig. 4. Effect of contact angle on the error of the curvature measurements.

the surface condition as a result of local contamination, non-uniform temperature and concentration.

3.1. Effect of wavelength

The red ($\lambda = 435.8$ nm), green ($\lambda = 543.5$ nm), or blue ($\lambda = 656.3$ nm) monochromatic wavelengths from a Hg arc lamp with a filter can be easily used in our optical system. Since the intensity of the light source is a function of wavelength, an understanding of its effect on the error would be useful for the design of the optical system. In Fig. 3, the curves for these frequencies are obtained for pentane by setting $m = 0$ (the zeroth order fringe) and $n = 8$ (the 8th order fringe) in Eq. (14). It is clearly seen that the error increases as the wavelength decreases (from the red to the blue).

The smallest film thickness can be obtained by using blue light since the thickness of the zeroth dark fringe is 0.08 μm. However, the contrast, which is used to denote the degree of difference between the brightest and darkest components in an image in our experimental system, is the lowest for blue among three wavelengths. The contrast affects the ability to locate the center of the fringe. Red light has the highest contrast, but the thickness of the zeroth dark fringe is 0.12 μm. Therefore, it can not be used to measure thickness as small as that measured by blue light. For green light, the smallest measurable thickness and the fringe contrast are in between those associated with the blue and red frequencies. We note that the error for the green frequency is also in between the errors for the blue and red frequencies. Balancing these factors, the green light frequency was chosen for illumination in our optical system. Hence, it is also chosen for the subsequent error analysis.

3.2. Effect of the number of dark fringes

If the resolving power of the system is fixed, the number of interference fringes observed is smaller for the meniscus with the larger curvature. Hence, we estimate the error with $m = 0$ and $n = 4$ in Eq. (14) as an example for fewer fringes, $n = 8$ for the medium number of fringes, and $n = 16$ for more fringes. Fig. 3 shows a comparison of the estimated errors for pentane with green light. The plot clearly demonstrates that the error increases when fewer fringes are used to obtain the curvature. This analytical result indicates that the error can be reduced significantly by obtaining more fringes, which can be achieved by using a higher magnification objective.

3.3. Effect of the apparent contact angle and refractive index

For a completely wetting pentane meniscus, the apparent contact angle at $\delta = 0$ obtained using the extrapolated profile for a constant curvature is zero. For a partially wetting fluid, the apparent contact angle at $\delta = 0$ is greater than zero. The ethanol/glass system can be made partially wetting by heating the glass to a high temperature during fabrication of the cell. Fig. 4 shows the effect of the apparent contact angle on the errors for ethanol with green light. As expected, the error increases with the apparent contact angle. We note that for a zero contact angle, the error increases monotonously with increasing curvatures. However, for a relatively large contact angle, the error also increases with decreasing curvature in the region of small curvatures. Since the refractive index of completely wetting pentane (1.358) and partially wetting ethanol (1.359) are very close, changing the fluid has almost no effect on the error for a given K with $\theta = 0$.

4. Results and discussions

Using a conventional microscope light source projected through the objective, monochromatic light from a Hg arc with a narrow band filter (545.3 nm) was used to illuminate the cell at normal incidence of one side. The reflected interference patterns were viewed and captured by a CCD camera attached to the microscope, then digitized and stored. The stored images were later processed to yield plots of grey value versus distance. The grey value plots were further analyzed to obtain the film thickness profile as described by Das-Gupta et al. [31]. With a 50× objective, each of the 640×480 pixels of the camera measures the average reflectivity (thickness) of a region with a diameter of 0.1777 μm.

4.1. Isothermal CVB

The meniscus in the corner can be divided into three regions [2]: (1) the intrinsic meniscus region where the liquid film is thick and capillarity dominates. In this thick region, the curvature, at a particular axial position, is approximately constant when viscous losses due to flow towards the contact line are small at low evaporation rates; (2) the transition region ($\delta_0 \leqslant \delta \leqslant 0.1$ μm), where the liquid film becomes thin and both capillarity and disjoining pressure are important. Therefore, the curvature varies significantly in the transverse direction even at equilibrium; and (3) the equilibrium adsorbed thin film region, δ_0, where the film becomes extremely thin, the disjoining pressure dominates, and the curvature is approximately zero on a flat surface. The curvature can be treated as a constant only in a portion of the intrinsic meniscus region at equilibrium or at lower evaporation rates. For green light, the thickness of the zeroth dark fringes is 0.1 μm. The disjoining pressure may slightly affect the curvature of the film near 0.1 μm. Therefore, if the data fitting includes the zeroth dark fringe, the deviation of the calculated values from the experimental data may be larger compared to that without the zeroth dark fringe. To measure this deviation, the accuracy of the data fitting, Ac, is defined as

$$Ac = \frac{\sum_{i=1}^{N} \frac{|\delta_{\mathrm{theo},i} - \delta_{\mathrm{exp},i}|}{\delta_{\mathrm{exp},i}}}{N}, \tag{17}$$

where $\delta_{\mathrm{theo},i}$ is the calculated value obtained from Eq. (12), $\delta_{\mathrm{exp},i}$ is the experimental film thickness data, and N is the total number of dark and bright fringes used to obtain the curvature. Since Eq. (12) is obtained based on the assumption of the constant curvature of the film profile, the value of Ac will become larger if the data fitting includes the region where the curvature varies. Since we can change the region of the data fitting, Eq. (17) can be used to determine the region where the disjoining pressure and/or curvature gradient plays an important role. Fig. 5 shows interference fringes in the corner of the cell obtained using pentane under isothermal condition. The comparison of the experimental data and theoretical film profile of pentane under equilibrium conditions are shown in Fig. 6. In Fig. 6, the theoretical film profile was obtained by best fitting the experimental film thickness above 0.3 μm (from the first to the seventh dark fringe) with plus signs representing the dark and bright fringes. The calculated values have an excellent agreement with the experimental data ($Ac = 0.58\%$), which indicates that the film above 0.3 μm has a constant curvature of 9115 m^{-1}. The curvature obtained from the fitting of data above 0.1 μm (from the zeroth to the seventh dark fringe) is 8930 m^{-1}. The deviation from experimental data increases to 1.93%, which is three times larger than the previous fitting. It indicates that the curvature may vary near the region of 0.1–0.3 μm due to the disjoining pressure or a very small evaporation/condensation process. At $\delta = 0.1$ μm, the ratio of disjoining pressure to capillarity is approximately 0.001. Thus, we can conclude that additional phenomena have a small effect in the region 0.1–0.3 μm.

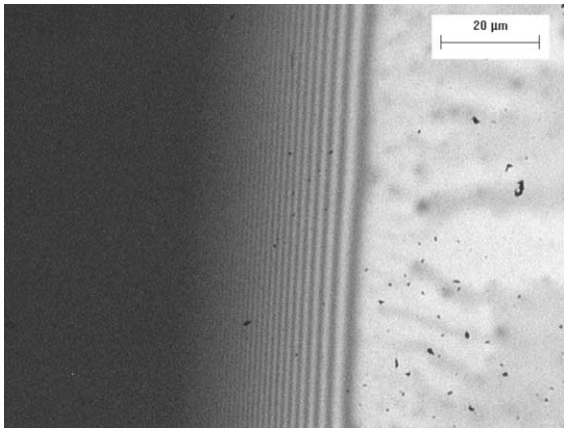

Fig. 5. Interference fringes of pentane with a low evaporation corresponding to Curve I in Fig. 8.

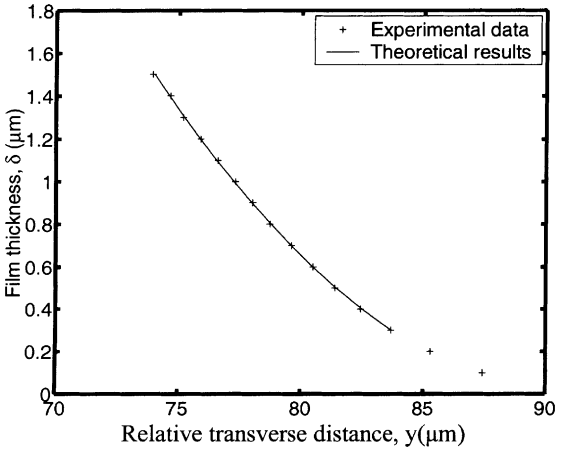

Fig. 6. Comparison of the experimental film profile with theoretical results using first to seventh dark fringes with an accuracy of 0.58%.

Fig. 7 shows that experimental pentane curvatures were in good agreement with theoretical hydrostatic results in the vertical isothermal CVB with a bubble length of 22 mm. Circle signs represent measured curvatures in the region where $\delta \geqslant 0.1$ μm, and the straight line was obtained from Eq. (6). The curvature increases with l, which provides the capillary pressure difference to balance the hydrostatic pressure. Note that the intercept

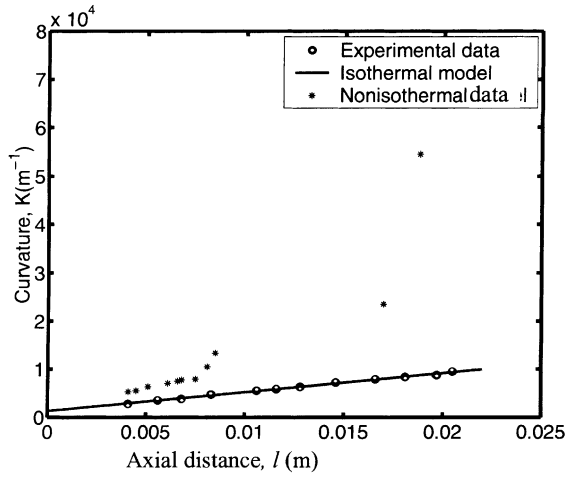

Fig. 7. Curvatures profiles of isothermal and non-isothermal pentane.

at $l = 0$ represents the curvature K_b at the base of the CVB and the slope of the straight line is $-(\rho_l g/\sigma_l)$ with $g < 0$. The star signs in Fig. 8 represent curvatures of the non-isothermal CVB where the curvature gradient is much larger due to evaporation/condensation.

4.2. Non-isothermal CVB

For a 20 mm long CVB of pentane shown in Fig. 1, the junction of the evaporator and condenser regions is located at $x = 16.9$ mm with a heat flux at the top of the glass of 0.39 W. Fig. 8 shows the film profiles at different locations in the evaporator along the axial length of the CVB, which represent different local evaporation rates and hydrostatic heads. For comparison, the four curves

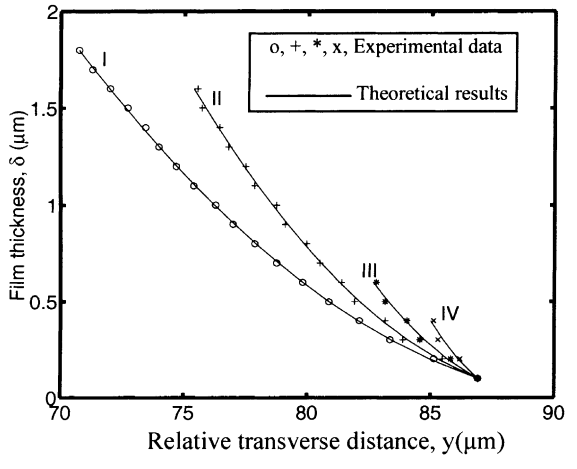

Fig. 8. Comparison of the film profiles at different axial positions.

are shifted to have the same location of the zeroth dark fringe, 0.1 μm. The solid lines represent the theoretical results based on Eq. (14). Curve I, located at 16.4 mm, is the film profile close to the junction. Fig. 5 shows the interference fringes of Curve I, where the number of clearly discernible dark fringes is 9. The curvature is 7532 m^{-1}, and the theoretical error associated with the resolution is $E_r = 2.1\%$. The accuracy of fitting is $Ac = 0.42\%$.

Curves II and III are closer to the heater, located at 14.5 and 6 mm with $K = 1.335 \times 10^4$ and $K = 2.35 \times 10^4$ m^{-1}, respectively. As curvature increases, the film profile become steeper and the spacing between fringes decreases significantly. The number of dark fringes available for the data fitting decrease, and are 8 for Curve II and 3 for Curve III. The errors for the curvature measurements are $E_r = 3.0\%$ for Curve II and $E_r = 8.3\%$ for Curve III. The accuracies of data fitting are $Ac = 2.5\%$ for Curve II and $Ac = 4.0\%$ for Curve III.

Curve IV is 4.2 mm from the top, close to the dry region, and only an extremely thin film exists on the flat surface with a small meniscus in the corner. Only two dark fringes are observable interference fringes are very few. The curvature is 5.45×10^4 m^{-1}, which is the upper limit of curvature measurements using our current optical system. The error and the accuracy of data fitting are relatively large, $E_r = 18.2\%$ and $Ac = 6.1\%$, which can be reduced by using a higher resolution CCD camera.

In the evaporator region, the curvature of the meniscus in the corner increases from 7532 to 5.45×10^4 m^{-1} as the location of the corner becomes closer to the heater. The resulting pressure gradient in the fluid drives the fluid from the region of condensation towards the region of evaporation. These curvature values are compared with the isothermal values in Fig. 7. Note that the apparent contact angles (θ_c) of all four curves in Fig. 8 are zero. This is not obvious in the figure because of the different scales in the axes.

Fig. 9 shows a comparison of film profiles of evaporation and condensation. The signs of plus and circle denote the experimental data, and the solid lines represent the theoretical values based on constant K. The profile for evaporation is Curve I, located at 16.4 mm, in Fig. 5 with $K = 7532$ m^{-1}. The curve for condensation is located at 18.9 mm from the top. It has a constant curvature of 5337 m^{-1} for the film above 0.4 μm, and the accuracy of the data fitting is 0.61%, which is very good. When the data near 0.1 μm are included, the error increases to 3.77% due to the thicker condensate film on the flat surface of the CVB cell. Since the film near 0.1 μm was changed by condensation, the constant curvature assumption is valid only above 0.4 μm. The change in curvature for $\Delta x = 2.4$ mm due to hydrostatics is $\Delta K = 945$ m^{-1} whereas the difference between

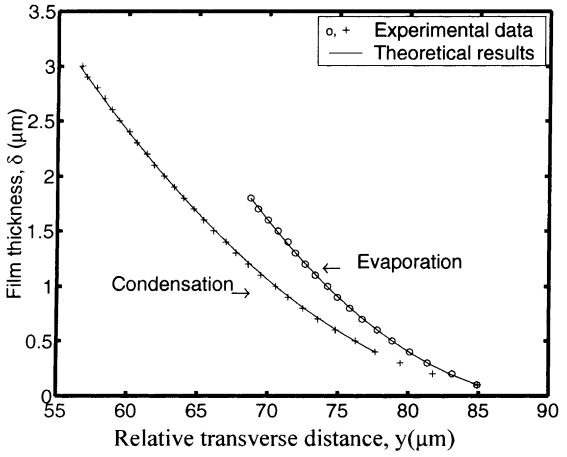

Fig. 9. Comparison of condensation and evaporation film profiles.

these two non-isothermal profiles is $\Delta K = 2195\ \mathrm{m}^{-1}$. We also find that the error in the profile with evaporation is relatively large (2.1%) although the curvature is relatively small, which indicates an effect due to viscous losses.

Theoretically, Swanson and Herdt [11] found that a change in dispersion constant produces a noticeable change in the meniscus profile only at the microscopic level near the tube wall and that the local capillary pressure remained constant. We note that Cook et al. [20] did not have a constant curvature in their measurements on an immersed flat plate because the upstream boundary condition was a flat pool of liquid.

5. Conclusions

- An improved image analyzing technique was developed to obtain simultaneously the curvature and the apparent contact angle of a liquid film.
- Experimental film profiles with values of the curvature in the range of $7532\ \mathrm{m}^{-1} \leqslant K \leqslant 5.45 \times 10^4\ \mathrm{m}^{-1}$ were measured.
- A theoretical analysis shows that the error associated with the system resolution increases as the curvature increases; the apparent contact angle increases; the wavelength decreases; and the number of dark fringes used for the data fitting decreases.
- Experimental results show that Eq. (13) describes the film profile in the thicker portion of the meniscus very well, within an accuracy of 1% when the curvature is constant.
- The accuracy of data fitting based on the assumption of a constant curvature can be used to determine the region where the disjoining pressure or viscous flow affects the profile.
- Experimental results show that error, E_r, increases as the curvature increases in the evaporator, and that E_r in the thicker region of condensation is lower than that in the region of evaporation.
- In small regions, the effect of pressure changes is easier to measure than the effect of temperature changes.

Acknowledgements

This material is based on work supported by the National Aeronautics and Space Administration under grant # NAG3-2351. Any opinions, findings, and conclusions or recommendations expressed in this publication are those of the authors and do not necessarily reflect the view of NASA.

References

[1] B.V. Derjaguin, S.V. Nerpin, N.V. Churaev, Effect of film transfer upon evaporation of liquids from capillaries, Bull. Rilem 29 (1965) 93–98.
[2] M. Potash Jr., P.C. Wayner Jr., Evaporation from a two-dimensional extended meniscus, Int. J. Heat Mass Transfer 15 (1972) 1851–1863.
[3] P.S. Ayyaswamy, I. Catton, D.K. Edwards, Capillary flow in triangular grooves, J. Appl. Mech. 41 (1974) 332–336.
[4] Y. Kamotani, Evaporator film coefficients of grooved heat pipes, in: Proceedings of the Third International Heat Pipe Conference, American Institute of Aeronautics and Astronautics, 1978, pp. 128–130.
[5] F.J. Renk, P.C. Wayner Jr., An evaporating ethanol meniscus, part II: analytical studies, J. Heat Transfer 101 (1979) 59–62.
[6] P.C. Wayner Jr., Y.K. Kao, L.V. LaCroix, The interline heat transfer coefficient of an evaporating wetting film, Int. J. Heat Mass Transfer 19 (1976) 487–492.
[7] F.W. Holm, S.P. Goplen, Heat transfer in the meniscus thin film region, J. Heat Transfer 101 (1979) 543–547.
[8] A.V. Mirzamoghadam, I. Catton, A physical model of the evaporating meniscus, J. Heat Transfer 110 (1988) 201–207.
[9] X. Xu, V.P. Carey, Film evaporation from a micro-grooved surface-an approximate heat transfer model and its comparison with experimental data, J. Thermophys. 4 (1990) 512–520.
[10] P. Stephan, C.A. Busse, Analysis of the heat transfer coefficient of grooved heat pipe evaporator walls, Int. J. Heat Mass Transfer 35 (1992) 383–391.
[11] L.W. Swanson, G.C. Herdt, Model of the evaporating meniscus in a capillary tube, J. Heat Transfer 114 (1992) 434–441.
[12] J.R. Brown, W.S. Chang, heat transfer from stable evaporating thin films in the neighborhood of a contact line, in: National Heat Transfer Conference, Atlanta, Georgia, 1993.

[13] S. DasGupta, I.Y. Kim, P.C. Wayner Jr., Use of the Kelvin–Clapeyron equation to model an evaporating curved microfilm, J. Heat Transfer 116 (1994) 1007–1015.
[14] L.W. Swanson, G.P. Peterson, The interfacial thermodynamics of micro heat pipes, J. Heat Transfer 115 (1995) 195–201.
[15] P.C. Wayner Jr., Intermolecular forces in phase-change heat transfer: 1998 kern award review, AIChE J. 45 (1999) 2055–2068.
[16] R.R. Sharp, The nature of liquid film evaporation during nucleate boiling, NASA-TN-D1997, Washington, DC, 1964.
[17] H.H. Jawurek, Simultaneous determination of microlayer geometry and bubble growth in nucleate boiling, Int. J. Heat Mass Transfer 12 (1969) 843–848.
[18] C.M. Voutsinos, R.L. Judd, Laser interferometric investigation of the microlayer evaporation phenomena, J. Heat Transfer 97 (1975) 88–93.
[19] F.J. Renk, P.C. Wayner Jr., An evaporating ethanol meniscus, part I: experimental studies, J. Heat Transfer 101 (1979) 55–58.
[20] R. Cook, C.Y. Tung, P.C. Wayner Jr., Use of scanning microphotometer to determine the evaporative heat transfer characteristics of the contact line region, J. Heat Transfer 103 (1981) 325–330.
[21] P.C. Wayner Jr., C.Y. Tung, M. Tirumala, J.H. Yang, Experimental study of evaporation in the contact line region of a thin film of hexane, J. Heat Transfer 107 (1985) 182–189.
[22] A.V. Mirzamoghadam, I. Catton, Holographic interferometry investigation of enhanced tube meniscus behavior, J. Heat Transfer 110 (1988) 208–213.
[23] H.C. Chebaro, K.P. Hallinan, S.F. Kim, W.S. Chang, Evaporation from a porous wick heat pipe for non-isothermal interfacial conditions, in: National Heat Transfer Conference, Atlanta, Geogia, 1993.
[24] I.Y. Kim, P.C. Wayner Jr., Shape of an evaporating completely wetting extended meniscus, J. Thermophys. Heat Transfer 10 (1996) 320–325.
[25] M. Karthikeyan, J. Huang, J.L. Plawsky, P.C. Wayner Jr., Experimental study and modeling of the intermediate section of the nonisothermal constrained vapor bubble, J. Heat Transfer 120 (1998) 166–173.
[26] K.D. Kihm, D.M. Pratt, Contour mapping of thin liquid film thickness using fizeau interferometer, in: Proceedings of the 33rd National Heat Transfer Conference, Albuquerque, New Mexico, 1999, NHTC99-224.
[27] Y.-X. Wang, J. Plawsky, P.C. Wayner Jr., Heat and mass transfer in a vertical constrained vapor bubble heat exchanger using ethanol, in: Proceedings of the 34th National Heat Transfer conference, Pittsburgh, PA, 2000, NHTC2000-12201.
[28] Y.-X. Wang, J.L. Plawsky, P.C. Wayner Jr., Optical measurement of microscale transport processes in dropwise condensation, Microscale Thermophys. Eng. 1 (2001) 55–69.
[29] D. Khrustalev, A. Faghri, Thermal characteristics of conventional and flat miniature axially grooved heat pipes, J. Heat Transfer 117 (1995) 1048–1054.
[30] G.P. Peterson, J.M. Ha, Capillary performance of evaporating flow in micro grooves: an approximate analytical approach and experimental investigation, J. Heat Transfer 120 (1998) 743–751.
[31] S. DasGupta, J.L. Plawsky, P.C. Wayner Jr., Interfacial force field characterization in a constrained vapor bubble thermosyphon, AIChE J. 41 (1995) 2140–2149.
[32] A. Faghri, Heat Pipe Science and Technology, Taylor & Francis, Washington, DC, 1995.
[33] W.J. Yang, A. Nouri, Interfacial turbulence in minute drops evaporating on a flat plate, Lett. Heat Mass Transfer 8 (1981) 115–125.
[34] J.D. Chen, N. Wada, Edge profiles and dynamic contact angles of a spreading drop, J. Colloid Interface Sci. 148 (1992) 207–222.
[35] P.C. Wayner Jr., The effect of interfacial mass transport on flow in thin liquid films, Colloid Surf. 52 (1991) 71–84.
[36] L. Zheng, Experimental and theoretical investigations of a loop constrained vapor bubble, Ph.D candidacy proposal, Rensselaer Polytechnic Institute, Troy, NY, March 2001.